1 **Mie–Raman-Fluorescence lidar observations of aerosols during pollen season in the north of**

2 **France**

3 Igor Veselovskii[1], Qiaoyun Hu[2], Philippe Goloub[2], Thierry Podvin[2], Marie Choël[3], Nicolas Visez[4],

4 Mikhail Korenskiy[1]

5 *[1]Prokhorov General Physics Institute of the Russian Academy of Sciences, Moscow, Russia.*

6 *[2]Univ. Lille, CNRS, UMR 8518 - LOA - Laboratoire d'Optique Atmosphérique, Lille, 59000,*

7 *France*

8 *[3]Univ. Lille, CNRS, UMR 8516 - LASIR - Laboratoire de Spectrochimie Infrarouge et Raman,*

9 59000, Lille, France

10 *[4]Univ. Lille, CNRS, UMR 8522 - PC2A - Physicochimie des Processus de Combustion et de*

11 *l'Atmosphère, 59000, Lille, France*

13 **Abstract**

14 Multiwavelength Mie–Raman–fluorescence lidar of Lille University with the capability to

15 measure three aerosol backscattering, two extinction coefficients and three linear depolarization

16 ratios together with the fluorescence backscattering at 466 nm was used to characterize aerosols

17 during the pollen season in the north of France for the period March – June 2020. The results of

18 observations demonstrate that the presence of pollen grains in aerosol mixture leads to an increase

19 of the depolarization ratio. Moreover, the depolarization ratio exhibits a strong spectral

20 dependence increasing with wavelength, which is expected for the mixture containing fine

21 background aerosols with low depolarization and strongly depolarizing pollen grains. High

22 depolarization ratio correlates with the enhancement of the fluorescence backscattering,

23 corroborating the presence of pollen grains. Obtained results demonstrate that simultaneous

24 measurements of particle depolarization and fluorescence allows to separate dust, smoke particles

25 and aerosol mixtures containing the pollen grains.

27   **1. Introduction**

28   Pollen grains represent a significant fraction of primary biological particles emitted from the

29 biosphere into the atmosphere in certain seasons and locations (Fröhlich-Nowoisky et al., 2016).

30 There has been a growing interest in pollen study in recent years, because they can affect human

31 health by causing allergy-related diseases and contribute to the cloud formation by acting as giant

32   cloud condensation nuclei (CCN) (Diehl et al., 2001; Pope, 2010; D'Amato et al., 2014; Steiner et

33   al., 2015; Lake et al., 2017; Mack et al., 2020). To investigate the processes of pollen transport

34   and dispersion, the information about vertical distribution of pollen grains is needed, and this

35   information can be obtained from lidar measurements. Pollen grains are large irregularly shaped

36   particles of complicated morphology (Frenguelli, 2003), causing strong depolarization of the

37   backscattered laser radiation, which provides a basis for their identification. The first profiling of

38   pollen with depolarization lidar was reported by Sassen (2008, 2011). His measurements over

39   Alaska revealed that linear depolarization ratio of birch pollen plumes at 694 nm can exceed 30%.

40   Further studies of pollen with elastic backscatter lidar at 532 nm were reported by Noh et al. (2013

41   a,b) and by Sicard et al. (2016). Their measurements confirmed high depolarization ratio of pollen

42   grains (particle depolarization ratios as high as 43% were observed for aerosol mixture containing

43   *Platanus* and *Pinus* pollen). Moreover, pollen grains backscattering demonstrated strong diurnal

44   cycle, being highest near the noon. The use of multiwavelength observations increases capability

45   of lidar technique for aerosol characterization. In recent studies of Bohlmann et al. (2019) and

46   Shang et al., (2020) measurements performed with Polly[XT] lidar allowed to estimate mean values

47   of the lidar ratios (about 45 sr and 55 sr at 355 and 532 nm respectively for birch pollen grains).

48   The lidar measurement of pollen depolarization ratio at 355 nm, 532 nm and 1565 nm was reported

49   also in recent work of Bohlmann et al. (2020), revealing strong decrease of depolarization ratio at

50   355 nm.

51   Atmospheric biological particles efficiently produce wideband fluorescence emission,

52   when being exposed to UV radiation (Pohlker et al., 2012; Pan, 2015; Miyakawa et al., 2015),

53   which offers an opportunity for monitoring them with fluorescence lidars. Nowadays, lidar

54   spectrometers based on multianode photomultipliers allow a simultaneous detection of

55   fluorescence backscattering in 32 spectral bins (Sugimoto et al., 2012; Reichardt et al., 2014, 2017;

56   Saito et al., 2018; Richardson et all, 2019). In particular, such lidar spectrometer was used in recent

57   work of Saito et al. (2018) for remote measurement of the fluorescence spectrum of atmospheric

58   pollen grains. The results demonstrate that, for 355 nm stimulating wavelength, the fluorescence

59   spectra of different pollen grains have maxima in the 400–600 nm range and the intensity peak at

60   around 460 nm.

61   To achieve the highest sensitivity of fluorescence detection, in many tasks it is preferable

62   to use a single channel monitoring, where a part of the fluorescence spectrum is selected with a

63   wideband interference filter (Immler et al, 2005; Rao et al., 2018; Li et al., 2019). In our recent

64   publication (Veselovskii et al., 2020a) we reported the results obtained from a modified Mie–

65   Raman lidar system in Laboratoire d'optique Atmosphérique with one additional fluorescence

66   channel at 466 nm. Such an approach has proved high sensitivity, allowing to detect fluorescence

67   signals from weak aerosol layers and to calculate the fluorescence backscattering coefficient from

68   the ratio of fluorescence and nitrogen Raman backscatters, thus making it potentially attractive for

69   pollen monitoring.

70   In the present research we combine capability of multiwavelength Mie–Raman lidar for

71   providing three backscattering, two aerosol extinction coefficients and linear depolarization ratio

72   at three wavelengths with single channel fluorescence measurements for characterization of

73   aerosol mixtures containing pollen grains. The measurements reported were performed during

74   March–June 2020 period at the Lille Atmospheric Observation Platform (https://www-loa.univ-

75   lille1.fr/observations/plateformes.html?p=apropos)   hosted   by   Laboratoire   d'Optique

76   Atmospherique, University of Lille, Hauts-de-France region.

77

78   **2. Instrumentation**

79   **2.1 Mie-Raman-Fluorescence lidar**

80   The measurements were performed using LILAS (LIlle Lidar AtmosphereS) system – a

81   multiwavelength Mie-Raman lidar, based on a tripled Nd:YAG laser with a 20 Hz repetition rate

82   and pulse energy of 70 mJ at 355 nm. The backscattered light is collected by a 40 cm aperture

83   Newtonian telescope. The full geometrical overlap of the laser beam and the telescope FOV is

84   achieved at approximately 1000 m and to obtain the information about particles at lower altitudes,

85   part of the measurements were performed at an angle of 30 degrees to the horizon. No overlap

86   correction of lidar signals was performed. The system is designed for a simultaneous detection of

87   elastic and Raman backscattering, allowing the so called $3\beta+2\alpha+3\delta$ data configuration, including

88   three particle backscattering (β_{355}, β_{532}, β_{1064}), two extinction (α_{355}, α_{532}) coefficients along with

89   three particle depolarization ratios (δ_{355}, δ_{532}, δ_{1064}). The particle depolarization ratio δ, determined

90   as a ratio of cross- and co-polarized components of the particle backscattering coefficient, was

91   calculated and calibrated the same way as described in Freudenthaler et al. (2009). The description

92   of the system can be found in the recent publication of Hu et al., (2019).

93   To perform fluorescence lidar measurements, the water vapor Raman channel at 408 nm

94   was replaced by a fluorescence channel, whose spectrum is captured by a wideband filter centered

95   at 466 nm and of 44 nm width (Veselovskii et al., 2020a). The fluorescence measurements were

96   performed during night time only. The aerosol extinction and backscattering coefficients at 355

97   and 532 nm were calculated from Mie-Raman observations (Ansmann et al., 1992), while β_{1064}

98   was derived by the Klett method (Klett, 1985). The fluorescence backscattering coefficient β_F is

99   calculated from the ratio of fluorescence and nitrogen Raman backscattering, as described in

100   Veselovskii et al. (2020a). This approach allows to evaluate the absolute values of β_F, if the relative

101   sensitivity of the channels is calibrated and the nitrogen Raman scattering cross section is known.

102   Corresponding uncertainty we estimate to be below 50%. Parameters of detectors were not

103   changed during the campaign, so uncertainty of relative variations of β_F was significantly lower

104   and was determined by the statistical errors of fluorescence measurements.

105   To characterize the efficiency of the fluorescence in respect to elastic scattering, the

106   fluorescence capacity

107   $$G_F = \frac{\beta_F}{\beta_{532}} \qquad\qquad (1)$$

108   is also used. This parameter depends on the relative humidity (RH), so information about RH is

109   important for data analysis. Radiosonde measurements are used to monitor water vapor, as the

110   water vapor channel is replaced by the fluorescence channel in current lidar configuration. The

111   closest available radiosonde data are from Herstmonceux (UK) and Beauvecchain (Belgium)

112   stations, located 160 km and 80 km away from the observation site respectively. These radiosonde

113   data are not collocated with the lidar measurements, so only qualitative analysis of humidification

114   effects was possible.

115

116   **2.2 Pollen in situ sampling**

117   Airborne pollen grains and spores were collected by a Hirst-type volumetric sampler

118   (VPPS 2000, Lanzoni s.r.l). The pollen sampler was located on the campus of the University of

119   Lille (France) on the rooftop of a 20-m-high building where the lidar instrument was operated.

120   Ambient air was sampled at 10 L.min^{-1} flow rate, allowing the impaction of pollen and spores on

121   an adhesive strip mounted on a rotating clockwork-driven drum. The impaction surface moves at

122   2 mm.h^{-1} behind the entrance slit, allowing a temporal resolution of 2 hours. The adhesive strip

123   was substituted every 7 days after a full rotation of the drum, which is splitted into 7 parts, each

124   corresponding to a day of monitoring. And then they are fixed on a microscope glass slide with

125   gelatin and fuchsine dye. Pollen taxa were identified by light microscopy on the basis of their

126   characteristic shape and size. Airborne pollen concentrations were expressed as a daily and dual

127   hourly number of pollen grains per cubic meter of air.

128   Fig.1 shows the most abundant pollen taxa for the period from March to June 2020 in Lille.

129   These include: *Betula* (54.8% of total pollen taxa over the period), *Fraxinus* (8.2%), *Quercus*

130   (5.8%), *Urticaceae* (4.6%), *Salix* (4.5%) and *Cupressaceae* (4.1%). The same figure shows also

131   the fluorescence backscattering β_F measured by lidar. The results presented are obtained by

132   averaging all available data during the night and the maximal values in $500 - 1000$ m height range

133   are shown. The highest fluorescence was observed in the end of March, when ash (*Fraxinus*) is

134   the main pollinator. The period of intense birch (*Betula*) pollination (3-15 April 2020) correlates

135   also with high β_F. Strong fluorescence observed for 5-10 May and 28 May–2 June periods, can be

136   due to grass (*Poaceae*) pollen contribution. By the end of June, β_F decreases and becomes

137   comparable with fluorescence backscattering of background aerosol. From Fig.1, we can conclude

138   that there is no direct correlation between in situ and fluorescence lidar measurements, thus pollen

139   observed in the boundary layer by the lidar are probably transported from other regions.

140   Comparing lidar and in situ observations, we should also keep in mind, that maximum of pollen

141   emission occurs near the noon, while lidar measurements were performed in the night.

142

143   **3. Discrimination of pollen from other types of aerosol**

144   *3.1. Specific features of pollen containing aerosol mixture*

145   In contrast to the observations performed over Alaska (Sassen, 2008, 2011) or in Kuopio,

146   Finland (Bohlmann et al., 2019), where pollen concentration was high due to boreal forests

147   surrounding, the pollen loading in the north of France is significantly lower. Long-term lidar and

148   sun photometer observations performed at Lille University demonstrate that local aerosol is mainly

149   of continental type, with predominance of the fine mode particles and low depolarization ratio.

150   The emission of large pollen grains, should lead to strong spectral dependence of the depolarization

151   ratio, because the backscattering at 1064 is less sensitive to the fine background particles than at

152   shorter wavelengths, thus particle depolarization ratio at 1064 nm (δ_{1064}) should be more sensitive

153   to the presence of pollen grains, compared to δ_{355} and δ_{532}. The particle depolarization ratio δ of

154   the mixture, containing background aerosol (*b*) and pollen (*p*), with corresponding depolarization

155   ratios δ^b and δ^p, can be calculated as:

156 $$\delta = \frac{\left(\dfrac{\delta^p}{1+\delta^p}\right)\beta^p + \left(\dfrac{\delta^b}{1+\delta^b}\right)\beta^b}{\dfrac{\beta^p}{1+\delta^p} + \dfrac{\beta^b}{1+\delta^b}} \qquad (2)$$

157   Here total backscattering $\beta = \beta^b + \beta^p$.

158   To estimate the dependence of depolarization of the aerosol mixture on the contribution of

159   pollen to the backscattering coefficient $\dfrac{\beta^p_{532}}{\beta_{532}}$ at 532 nm, a simplified simulation was performed.

160   Assuming that the depolarization ratios of pollen and background aerosol are spectrally

161   independent and that δ^p=30% while δ^b=3%, the mixture depolarization ratios δ_{355}, δ_{532}, δ_{1064} were

162   calculated as a function of $\dfrac{\beta^p_{532}}{\beta_{532}}$ using expression (2). For pollen the backscattering Angstrom

163   exponents (BAE) $A^\beta_{355/532} = A^\beta_{532/1064} = 0$ were used. The backscattering Angstrom exponents of

164   background aerosol are assumed to be the same for both wavelength pairs ($A^\beta_{355/532} = A^\beta_{532/1064}$), and

165   computations were performed for the values of BAE A^β=1.0, 1.5, 2.0. Results of simulation are

166   shown in Fig.2. For low pollen contribution the depolarization ratio δ_{1064} increases faster with

167      $\dfrac{\beta^p_{532}}{\beta_{532}}$, comparing to δ_{532} and δ_{355}, and the slop of this increase depends on the BAE value. Spectral

168   properties of the real mixture can be more complicated, due to possible spectral dependence of

169   both δ^p and δ^b. Information on laboratory measured spectral dependence of depolarization ratios

170   of pollen is rare. Cao et al. (2010) measured the linear depolarization ratio of several types of

171   pollen in a chamber at 355, 532 and 1064 nm wavelengths. The results demonstrate strong

172   variation of spectral dependence for different taxa, and for most of the samples δ_{532} exceeded both

173   δ_{355} and δ_{1064}. In particular, for birch pollen, depolarization ratios at 355 nm, 532 nm and 1064 nm

174   are of 8%, 33% and 28%. Using the depolarization ratios from Cao et al. (2010) in analysis, we

175   should also keep in mind that measurements in the chamber were performed at low RH, and

176   depolarization ratios at higher RH may be different.

177   The Angstrom exponents $A^{\beta}_{355/532}$ and $A^{\beta}_{532/1064}$ depend on the particle size and the refractive

178   index in different way (Veselovskii et al., 2015), so their values can be different. Thus spectral

179   dependence of depolarization ratio of aerosol - pollen mixture will differ from simplified modeling

180   shown in Fig.2. However, for moderate contribution of pollen to the total backscattering ($\frac{\beta^{p}_{532}}{\beta_{532}}$

181   below ≈0.5), the depolarization ratio at 1064 nm should be higher than that at shorter wavelengths.

182   Hence, increase of the particle depolarization ratio with wavelength can be an indication of the

183   presence of large, irregularly-shaped pollen grains in aerosol mixture.

184   The presence of pollen should lead also to the decrease of the extinction and backscattering

185   Angstrom exponents. Extinction Angstrom exponent (EAE) depends mainly on particle size, while

186   BAE is sensitive also to the particle complex refractive index and shape, thus the measured profiles

187   of EAE and BAE can present significant difference (Veselovskii et al., 2015, 2020b). In our study

188   we analyze the EAE and BAE for the wavelength pair 355/532 nm ($A^{\alpha}_{355/532}$ and $A^{\beta}_{355/532}$) only,

189   because the extinction and backscattering coefficient involved are calculated from Mie–Raman

190   observations.

191   When analyzing Mie-Raman-fluorescence lidar measurements of pollen containing aerosol

192   mixtures, the numerous factors should be taken into account. These factors include the

193   fluorescence of background aerosol and other non-pollen aerosols that have strong fluorescence

194   capacity, for example, smoke particles. Dust particles can contribute to the increase of

195   depolarization ratio and, finally, the hygroscopic growth can modify the particle parameters. All

196   these factors will be considered in following sections.

197

198   ***3.2. Characteristics of background aerosol over observation site.***

199   Long-term observations in Lille University demonstrate that aerosol over the observation

200   site is mainly of continental type with predominance of the fine mode particles. Typical vertical

201   profiles of the background aerosol parameters, observed on 3 June 2020, are given in Fig.3,

202   showing aerosol elastic and fluorescence backscattering coefficients, lidar ratios, Angstrom

203   exponents and depolarization ratios at three wavelengths. The RH from Beauvecchain (Belgium)

204   radiosonde observations, was below 50% in the height range considered. Particle depolarization

205   ratios at all three wavelengths are below 7%, indicating that contribution of pollen to the total

206 backscattering was low. This agrees with the low values of pollen concentration provided by in
207 situ measurements (Fig.1). The lidar ratios at both wavelengths (S_{355}, S_{532}) are close, varying in
208 the 50-60 sr range, and the fluorescence capacity G_F is below 0.35×10^{-4}. The EAE and BAE
209 ($A^{\alpha}_{355/532}$, $A^{\beta}_{355/532}$) are in the 1.5–2.0 range. The presence of pollen should lead to a deviation of the
210 particle intensive parameters, such as the fluorescence capacity, depolarization ratio, EAE and
211 BAE, from the typical values of background aerosol.
212
213   *3.3 Identification of the smoke particles*
214   During the observation period the smoke elevated layers transported over Atlantic were
215 frequently detected. Smoke particles, are characterized by high fluorescence cross section
216 (Reichardt et al., 2017; Veselovskii et al., 2020a) and can interfere pollen fluorescence
217 measurements. The temporal evolution of the range corrected lidar signal, volume depolarization
218 ratio at 1064 nm and fluorescence backscattering for the smoke episode on the night 23 – 24 June
219 2020 are shown in Fig.4. During the night the smoke layer with low depolarization and high
220 fluorescence is observed at approximately 5000 m height. Back trajectories (not shown) indicate
221 that the layer is transported from Canada. Vertical profiles of the particle parameters for this
222 episode are shown in Fig.5. The lidar ratio is about 50 sr at 355 nm, while the lidar ratio at 532 nm
223 increases within the smoke layer from 60 sr to 80 sr. This increase of S_{532} occurs simultaneously
224 with decrease of $A^{\alpha}_{355/532}$ from 1.5 to 0.75, indicating that the particle size inside the layer growths
225 with height. Higher values of S_{532} in respect to S_{355} are typical characteristics for the aged smoke
226 (e.g. Müller et al., 2005; Nicolae et al., 2013; Hu et al., 2019). The depolarization ratio decreases
227 with wavelength from δ_{355}=10% to δ_{1064}=1.5%. Strong spectral dependence of depolarization ratio
228 and, in particular, low values of δ_{1064}, are the features, allowing to identify the smoke layers. We
229 should recall also, that increase of the particle depolarization ratio at 355 nm is more typical for
230 the aged smoke layers in the high troposphere (Haarig et al., 2018), though we observed this
231 increase at lower altitudes over Lille during smoke episodes in Summer – Autumn 2020.
232   The extinction Angstrom exponent $A^{\alpha}_{355/532}$ in the center of layer is about 0.75, while
233 $A^{\beta}_{355/532}$ is about 1.9 and shows no significant variation through the layer. High values of $A^{\beta}_{355/532}$
234 compared to $A^{\alpha}_{355/532}$ is another feature that will be used for aged smoke discrimination. Smoke

235 fluorescence capacity is high, reaching up to $G_F=5*10^{-4}$ for the period of observations, and this is
236 one more feature, allowing to separate smoke from other types of aerosol.
237
238 ### 3.4 Identification of the dust particles
239   Presence of dust particles and pollen in the fine background aerosol leads to some common
240 characteristics in the lidar data, such as the decrease Angstrom exponents and increase of
241 depolarization ratios. However, pollen and dust can be separated by the fluorescence capacity. The
242 vertical profiles of particle parameters during dust episode on 27 May are shown in Fig.6. The dust
243 containing layer extends from 2000 m to 7000 m and the particle depolarization ratios δ_{1064} and
244 δ_{532} in this layer are close to 20%. These values are lower than depolarization of pure dust. For
245 example, Freudenthaler et al. (2009) for pure dust provide the values of 27% and 31% at 1064 nm
246 and 532 nm wavelengths respectively, thus in our case transported dust particles may be mixed
247 with local aerosols. The particle depolarization at 355 nm is not shown in the figure, because the
248 scattering ratio in the dust layer was too low to compute δ_{355} reliably. The fluorescence capacity
249 of particles in the dust layer is about 0.1×10^{-4} at 4000 m, which is factor 50 lower than G_F of the
250 smoke in Fig.5. There is also a weak aerosol layer at 1600 m with β_{532} about 0.035 $Mm^{-1}sr^{-1}$. The
251 fluorescence capacity in this layer is high ($G_F\approx2.0*10^{-4}$), suggesting that this layer may contain
252 smoke or pollen particles.
253
254 ### 3.5 Impact of particle hygroscopic growth
255   The vertical variation of observed aerosol properties may be a result of particle water
256 uptake, which should be separated from the features related to pollen presence. Fig.7 shows the
257 profiles of the particle parameters for the episode on 15 June 2020, when the aerosol hygroscopic
258 growth could take place. In the height range 900–1500 m the fluorescence backscattering β_F is
259 stable, while the elastic backscattering β_{532} increases by a factor 3. Radiosonde measurements in
260 Herstmonceux (UK) in this height range demonstrate an increase of RH from about 75% to 85%,
261 while lidar measured extinction and backscattering Angstrom exponents decrease from 1.5 to 1.3,
262 corroborating the presence the particle hygroscopic growth. The depolarization ratio δ_{1064} at low
263 altitudes exceeds δ_{355} and δ_{532}, which can be an indication of pollen presence. This is supported by
264 significant fluorescence capacity ($G_F=0.9\times10^{-4}$ at 750 m).

265   The number of fluorescent particles in the 900–1500 m range, does not present significant

266   changes (β_F is stable), so observed vertical variations, i.e. the decrease of depolarization ratios at

267   all three wavelengths and the increase of lidar ratios S_{355} and S_{532} from 50 sr to 65 sr, are probably

268   the result of water uptake by the particles. Water uptake does not change the number of fluorescent

269   molecules, however the fluorescence capacity decreases in the process of the hygroscopic growth,

270   so G_F can be a representative parameter of aerosol types only at the condition of low RH.

271

272   **4. Results of lidar measurements in the presence of pollen**

273   During March–June 2020, we had numerous measurement cases demonstrating the

274   features in the profiles of the particle parameters, that can be attributed to pollen. For representative

275   cases we have chosen observations with high depolarization ratio and high fluorescence

276   backscattering. The same time, we omitted the days with high relative humidity, to minimize the

277   impact of the hygroscopic growth effects. Below we consider several measurement cases

278   representing different scenarios, in particular, the episodes when pollen concentration decreases

279   with height (30-31 May, 1-2 June) and the episodes when pollen grains are well mixed inside the

280   boundary layer (27-28 March and 21 April).

281

282   *4.1. 30-31 May and 1-2 June 2020 observations*

283   The results of lidar measurements during the campaign in many episodes can be interpreted

284   as decrease of pollen concentration with height. Vertical profiles of the main particle parameters

285   for two representative cases in the nights of 30-31 May and 1-2 June 2020, are shown in Fig.8.

286   The atmospheric conditions for these nights were stable so the profiles presented are averaged over

287   approximately five hours interval. The HYSPLIT back trajectory analysis (Stein et al., 2015)

288   demonstrates that in 1000--2000 m height range the air masses were transported from the Northern

289   Europe. At the ground level, the grass could be the main pollen contributor for this period, as

290   shown in Fig 1. On 31 May (at 00:00 UTC) the RH measured by the radiosonde in Herstmonceux

291   (UK) was about 40% at 500 m and it increased up to 70% at 2000 m. On 2 June the RH increased

292   from approximately 40% to 60% in the same height range. For both nights the fluorescence

293   backscattering decreases with height, indicating the decrease of the concentration of fluorescent

294   particles (presumably pollen). This decrease of β_F correlates with decrement of the depolarization

295   ratio at all three wavelengths. Particle depolarization δ_{1064} is the highest (about 15% at 750 m),

296 while δ_{355} and δ_{532} are significantly lower. Such spectral dependence of depolarization ratio can

297 be partly due to the contribution of the background aerosol, as follows from model calculation in

298 Fig.2. The lidar ratios are available above 1250 m and for both cases, S_{355} and S_{532} increase with

299 height. It indicates that the lidar ratios of pollen in the two considered cases can be quite low:

300 below 40 sr at 355 nm and below 30 sr at 532 nm, considering that pollen concentration decreases

301 with height, which is inferred from the features of depolarization ratio and fluorescence

302 backscattering

303 The EAE for both nights varied in 1.75 - 2.0 range and did not show significant changes

304 with height. The BAE is lower (about 1.5 at 1000 m) and for both nights it shows some increase

305 in 1250–2250 m range. The BAE, in contrast to EAE, depends strongly on the particle refractive

306 index and shape, thus it may demonstrate higher sensitivity to the changes in aerosol mixture

307 composition. Recall that backscattering and extinction Angstrom exponents are related as:

308
$$A^{\beta}_{355/532} = A^{\alpha}_{355/532} + \frac{\ln(S_{532} / S_{355})}{\ln(355 / 532)} \tag{3}$$

309 Thus for $S_{355} > S_{532}$, which has been observed during pollen episodes, the $A^{\beta}_{355/532}$ is lower than

310 $A^{\alpha}_{355/532}$. This is in contrast with smoke episodes, where $S_{355} < S_{532}$ and $A^{\beta}_{355/532} > A^{\alpha}_{355/532}$ (Fig.5).

311 If the depolarization ratios of pollen δ^{p} and background aerosol δ^{b} are known, the pollen

312 backscattering coefficient β^{p} can be calculated. Such approach is widely used for the separation

313 of contributions of dust and smoke particles (Sugimoto and Lee, 2006; Tesche et al., 2009) and

314 the same technique was applied to separate pollen and background aerosol (Noh et al. 2013a;

315 Sicard et al., 2016; Shang et al., 2020). For height independent depolarization ratios of pollen and

316 background aerosol the pollen backscattering coefficient can be calculated as suggested by Tesche

317 et al. (2009):

318
$$\beta^{p} = \beta \frac{(\delta - \delta^{b})}{(\delta^{p} - \delta^{b})} \frac{(1 + \delta^{p})}{(1 + \delta)} \quad , \tag{4}$$

319 Here β and δ are backscattering coefficient and particle depolarization ratio of the mixture. The

320 profiles of β^{p}_{532} and the relative contribution $\dfrac{\beta^{p}_{532}}{\beta_{532}}$ are shown in Fig.8(b,e). Computations were

321 performed in assumption of height independent $\delta^{p}_{532} = 30\%$. For background aerosol, the values

322     $\delta_{532}^b = 3\%$ for 30-31 May and $\delta_{532}^b = 5\%$ for 1-2 June were used. On $30 - 31$ May contribution of

323   pollen $\dfrac{\beta_{532}^p}{\beta_{532}}$ at 750 m is estimated as 30%.

324   The profiles of β_F and β_{532}^p in Fig.8(b, e) behave similarly, decreasing with height. Above

325   2000 m the decrease of β_F slows down due to the fluorescence of background aerosol. The profiles

326   of the fluorescence capacity G_F and relative contribution $\dfrac{\beta_{532}^p}{\beta_{532}}$ also demonstrate a good correlation.

327   Thus both depolarization and fluorescence techniques lead to the same conclusion: pollen

328   concentration in the boundary layer for the considered episodes decreases with height.

329

330   *4.2. 27 – 28 March and 21 April 2020 observations.*

331   According to the in-situ pollen sampling at rooftop level, the maximal pollen content was

332   detected during birch pollination period on 4–20 April. However, the maximal fluorescence

333   backscattering of lidar data was observed in the end of March, when sampling shows an increase

334   of ash (*fraxinus*) pollen emission. The temporal evolution of range corrected lidar signal, volume

335   depolarization ratio at 1064 nm and fluorescence backscattering on 27-28 March night is shown

336   in Fig.9. The main part of the aerosol is localized below 2000 m. The back trajectory analysis

337   demonstrates the air masses in this episode were transported from the East Europe. In contrast with

338   Fig.8, where fluorescence decreases with height, on 27 -28 March the fluorescent particles are

339   rather well mixed inside the PBL (planetary boundary layer). The fluorescence backscattering is

340   high, exceeding 2.5×10^{-4} Mm^{-1}sr^{-1} and the volume depolarization at 1064 nm is about 15%. The

341   vertical profiles of the particle parameters, averaged for period $19:20 - 04:30$ UTC, are shown in

342   Fig.10. In spite of temporal variations of the lidar signal and the fluorescence backscattering inside

343   the PBL (Fig.9), the averaged over night profiles of particle parameters are representative.

344   Radiosonde measurements (at both Beauvecchain and Herstmonceux sites) show that RH

345   gradually increased with height from approximately 40% to 70% in 500–1750 m range. The

346   depolarization ratios δ_{532} and δ_{1064} inside the PBL are close, which is in contrast with results in

347   Fig.8, where δ_{1064} exceeds δ_{532}. This difference can be due to the different types of pollen occured,

348   which is probably grass in Fig.8 and birch in Fig.10. Besides, the BAE in Fig.10 is lower than that

349   in Fig.8, which decreases the influence of background aerosol on the spectral dependence of the

350   depolarization ratio, as follows from Fig.2.

351   Both the fluorescence backscattering and depolarization ratios do not demonstrate strong

352   variations inside the 600–1500 m range. The maximum of fluorescence capacity exceeds 1.2×10^{-4},

353   which is significantly higher than G_F for background aerosol in Fig.3. The profiles of G_F and

354    $\dfrac{\beta_{532}^{p}}{\beta_{532}}$ behave reasonably similar, the slight decrease of $\dfrac{\beta_{532}^{p}}{\beta_{532}}$ with height in respect to G_F can be

355   due to dependence of depolarization ratio of pollen on RH.

356   Agreements between results obtained from depolarization and fluorescence techniques in

357   Fig.8,10, corroborates the suggestion that the observed fluorescence is mainly due to the presence

358   of pollen. However, in some episodes the particles with high fluorescence cross section, other than

359   pollen, could interfere. In particular, such interference occurred in 20-23 April 2020 period. Fig.11

360   shows the vertical profiles of particle parameters measured on 21 April. The depolarization ratio

361   δ_{1064}=22% at 750 m was one of the highest during campaign. The RH was low, increasing from

362   30% to 45% in 800–1500 m range, according to Herstmonceux radio sounding. The back trajectory

363   analysis demonstrates, that below 1500 m the air masses are transported from Spain, while at 2000

364   m the transportation is from the Northern Europe.

365   Fluorescence backscattering is stable in 500–1500 m range and the fluorescence capacity

366   at 1000 m is about 1.5×10^{-4}, which is a typical value for the pollen. However, above 1250 m G_F

367   starts to rise, reaching the value of 2.5×10^{-4} at 1750 m. Such high G_F is more typical for the smoke

368   particles. Depolarization ratio δ_{355} is about 15%, and this is higher than corresponding values

369   shown in Fig.8, 10, which again may corroborate the presence of smoke particles. We should recall,

370   that smoke particles are small, so, in contrast to pollen, their presence influences δ_{355} stronger than

371   δ_{1064}. The enhanced values of δ_{355} and G_F were observed during 20-23 April period, indicating to

372   the possible presence of the biomass burning particles in the aerosol mixture.

373

374   ***4.3. Separation of pollen and smoke layers***

375   During the campaign we observed narrow layers with strong fluorescence. Two examples

376   of such observations, in the nights 13-14 April and 16-27 May 2020, are shown in Fig.12. The

377   white arrows on this figure point to the fluorescent layers. On 13 April, a weak aerosol layer

378   ($\beta_{532}\approx0.6$ Mm^{-1}sr^{-1} for 23:00 – 00:00 UTC) is observed at the top of the PBL. This layer

379   demonstrates volume depolarization ratios about 10% and high fluorescence backscattering. On

380   26-27 May a weak layer with high fluorescence backscattering occurs between 3 km and 4 km.

381   However, in contrast with the first case, it has low depolarization ratio, so the layers may have

382   different nature. Fig.13 shows the vertical profiles of the particle parameters for these two cases.

383   On 13-14 April the fluorescence backscattering below 1000 m is stable, while β_{532} rises, which

384   can be the result of the particle water uptake. Above 1000 m, the depolarization ratio δ_{1064} increases

385   up to 8%. Results in Fig.13a are averaged over 21:15–00:40 UTC temporal interval, but peak

386   values of δ_{1064} between 23:00 and 00:00 exceeded 12%. Fluorescence backscattering increases

387   simultaneously with the depolarization. The aerosol backscattering coefficient of fluorescent layer

388   is too low for a reliable calculation of δ_{355} and δ_{532}, so only the profile of δ_{1064} is provided.

389   On 26-27 May the backscattering coefficient of the fluorescent layer at 3400 m is lower

390   than in Fig.13a ($\beta_{532} \approx 0.14$ Mm^{-1}sr^{-1}), so the depolarization ratio δ_{1064} can be calculated only in the

391   center of the layer and it is about 2%, which is significantly lower than that on 13-14 April.

392   However, the fluorescence capacity on 26-27 May is up to 3.5×10^{-4}, which is typical for smoke.

393   Thus, we can conclude that the fluorescent layer on 26-27 May contains the smoke particles, due

394   to high G_F and low δ_{1064}. On 13-14 April, the fluorescence capacity is significantly lower (about

395   0.9×10^{-4}) and depolarization ratio δ_{1064} exceeds 10%, which is more typical for pollen. Due to low

396   backscattering coefficients of the fluorescent layers in Fig.12, we are not able to provide a

397   complete set of intensive parameters, such as Angstrom exponents and particle depolarization

398   ratios at three wavelengths. However, based on the obtained fluorescence capacities and δ_{1064}

399   values, we conclude that the fluorescent layers probably contain pollen grain in Fig.12a, and smoke

400   particles in Fig.12b.

401

402   *4.4 Aerosol classification based on polarization and fluorescence measurements.*

403   Table 1 summarizes the results in the campaign, showing the aerosol parameters, such as

404   particle depolarization and lidar ratios, extinction Angstrom exponent, fluorescence backscattering

405   and capacity for several days in March–June 2020 observations period, when the contribution of

406   pollen to the total particle backscattering was significant. All available night observations were

407   averaged and results are given for heights with the highest particle depolarization. Lidar ratios

408   varied approximately in 40-70 sr range, wherein normally S_{355} is greater than S_{532}. It must be

409   emphasized that pollen lidar ratios may differ for different taxa and that the observed lidar ratios

410   are not attributed to pure pollen, but to the aerosol–pollen mixture, so the values provided are

411   influenced by the properties of background aerosol. Moreover, the shape of pollen grains depends

412   on RH, (Heidemarie et al., 2018), which may also lead to the variation of pollen lidar ratios. In

413   most of the cases, the depolarization ratio presents strong spectral dependence and increases with

414   wavelength. This spectral dependence is probably the result of mixing of strongly depolarizing

415   pollen grains with fine background aerosol. The maximal value of observed fluorescence capacity

416   of pollen-aerosol mixture is 1.6×10^{-4}, which is significantly higher than that of background aerosol,

417   but lower than fluorescence capacity of smoke.

418   The simultaneous observations of depolarization ratio and fluorescence capacity for

419   different types of aerosol are summarized by Fig.14. On this plot, particle depolarization δ_{532} is

420   plotted versus G_F. The diagram allows to separate four types of the particles: (i) dust particles –

421   high δ_{532} and low G_F; (ii) pollen – high δ_{532} and high G_F; (iii) smoke – low δ_{532} and high G_F; (iiii)

422   background aerosol (continental type) - low δ_{532} and low G_F. Points corresponding to the pollen

423   mixture provide extended pattern, because parameters depend on the concentration of pollen in the

424   aerosol mixture. The dust measurements are also scattered, because dust over the instrumentation

425   site is long transported and mixed with local aerosol. Minimum G_F for dust is about 0.1×10^{-4} while

426   for smoke maximal G_F is about factor 50 higher. The fluorescence capacity depends on the relative

427   humidity, so strong scattering of measurement points can be partly also due to RH variations.

428   Maximal values of G_F for pollen mixture were about 1.5×10^{-4}, and the corresponding

429   depolarization ratios δ_{532} are about 18%. Thus, assuming that depolarization ratio of pure pollen is

430   30%, we can expect G_F for pure pollen to be about 2.5×10^{-4}, which is comparable with values for

431   smoke.

432

433   **Conclusion**

434   We analyzed the measurements from a multiwavelength Mie-Raman-fluorescence lidar

435   during March–June 2020 in the north of France, to reveal the features that can be attributed to

436   pollen grains. The lidar system allowed to measure depolarization ratios at three wavelengths,

437   simultaneously with the fluorescence backscattering at 466 nm. In numerous episodes during the

438   campaign, high values of the particle depolarization ratio at 1064 nm, exceeding 15%, were

439   observed. Moreover, depolarization ratio had strong spectral dependence, being the highest at 1064

440   nm and lowest at 355 nm, which is expectable for big particles of irregular shape mixed with fine,

low depolarizing background aerosol. The increase of particle depolarization correlated with enhancement of the fluorescence backscattering corroborating that in these episodes we observed aerosol mixtures containing pollen.

The lidar ratios of aerosol–pollen mixtures observed during campaign varied in a wide range. At low altitudes, where particle presented strong depolarization and fluorescence, in many cases we observed lidar ratios below 40 sr at both wavelengths. However, we had also cases when the lidar ratios at both wavelengths were in 50–60 sr range. Thus, at the moment we are not capable to specify lidar ratios for pure pollen and additional measurement campaigns in the locations with high pollen content are strongly desirable.

Obtained results demonstrate, that simultaneous measurements of particle depolarization and fluorescence allows to separate dust, smoke particles and pollen grains. Moreover, the fluorescence measurements provide additional information that can be used in aerosol classification schemes. However, further studies are needed to make this technique applicable for the quantitative pollen characterization. In the data analysis it is important to account for the process of water uptake by the particles, because hygroscopic growth increases backscattering of background aerosol and influences the pollen grain shape. In the presented lidar configuration, the water vapor channel was absent and radiosonde RH data were not collocated with lidar, which prevented us from performing a quantitative analysis of the hygroscopic effects. Since December 2020, we recovered the water vapor channel in upgraded configuration of the lidar. Moreover, we added one more fluorescence channel centered at 549 nm, which will be used in the next pollen campaign in 2021. This additional channel should improve discrimination of the pollen from other aerosols. In coming campaign we will try to correlate our results with pollen concentration at different location in Europe by using the transport model, e.g. SILAM (System for Integrated modeLling of Atmospheric coMposition) (Sofiev et al, 2013, 2015). The use of this model should help in identification of pollen type in our observations.

Data availability. Lidar measurements are available upon request
(philippe.goloub@univ-lille.fr).

Author contributions. IV processed the data and wrote the paper. QH and TP performed the measurements. PG supervised the project and helped with paper preparation. MC and NV performed in situ pollen analysis and MK developed software for data processing.
.

474 *Competing interests*. The authors declare that they have no conflict of interests.

475

476 **Acknowledgement**

477 We acknowledge funding from the CaPPA project funded by the ANR through the PIA under

478 contract ANR-11-LABX-0005-01, the "Hauts de France" Regional Council and the European

479 Regional Development Fund (ERDF). The "Réseau National de Surveillance Aérobiologique"

480 (RNSA) and the "Association pour la Prévention de la Pollution Atmosphérique" (APPA) are

481 gratefully acknowledged for providing Hirst-collected pollen grains identification and for

482 assistance with the pollen data handling. Development of lidar retrieval algorithms was supported

483 by Russian Science Foundation (projects 16-17-10241 and 21-17-00114).

484

485

486

Table 1. Lidar measured aerosol parameters, such as particle depolarization ratios (δ_{355}, δ_{532}, δ_{1064}), lidar ratios (S_{355}, S_{532}), extinction Angstrom exponent ($A^{\alpha}_{355/532}$), fluorescence backscattering coefficient (β_F) and fluorescence capacity (G_F) for several days during March – June 2020 period, when contribution of pollen to the total particle backscattering could be significant.

Day	Height, m	δ_{355}, %	δ_{532}, %	δ_{1064}, %	S_{355}, sr	S_{532}, sr	$A^{\alpha}_{355/532}$	$\beta_F \ast 10^{-4}$, Mm^{-1}sr^{-1}	$G_{F\ast}10^{-4}$
27 Mar	1150	9	12	13	50	42	1.5	2.5	1.2
7 Apr	1150	13	13	13	60	60	1.25	1.0	1.3
8 Apr	1000	11	10	9	50	60	1.0	1.9	1.0
15 Apr	750	15	15	17	40	40	0.7	0.4	0.9
16 Apr	1250	15	15	15	-	-	-	0.6	1.6
19 Apr	650	8	10	14	58	48	1.35	1.2	0.9
20 Apr	1000	18	18	22	55	45	1.2	0.75	1.3
21 Apr	750	15	17	22	66	47	1.25	1.1	1.4
22 Apr	1000	18	18	22	70	55	1.2	0.9	1.5
23 Apr	1000	6	14	11	53	65	1.25	1.5	1.05
30 May	750	7	10	16	-	-	-	0.8	1.2
1 June	750	7	10	16	-	-	-	1.25	1.5

491
492

References

Bohlmann, S., Shang, X., Giannakaki, E., Filioglou, M., Saarto, A., Romakkaniemi, S. and Komppula, M.: Detection and characterization of birch pollen in the atmosphere using multi-wavelength Raman lidar in Finland, Atmos. Chem. Phys. 19, 14559–14569, 2019. doi.org/10.5194/acp-19-14559-2019.

Bohlmann, S., Shang, X., Vakkari, V., Giannakaki, E., Leskinen, A., Lehtinen, K., Pätsi, S., and Komppula, M.: Lidar Depolarization Ratio of Atmospheric Pollen at Multiple Wavelengths, Atmos. Chem. Phys. Discuss., https://doi.org/10.5194/acp-2020-1281.

Cao, X., Roy, G., and Bernier, R.: Lidar polarization discrimination of bioaerosols, Opt. Eng., 49, 116201, https://doi.org/10.1117/1.3505877, 2010.

D'Amato, P.G., Bergmann, K.C., Cecchi, L., Annesi-Maesano, I., Sanduzzi, A., Liccardi, G., Vitale, C., Stanziola, A., D'Amato, M.: Climate change and air pollution: Effects on pollen allergy and other allergic respiratory diseases. Allergo J 23, 32–38, 2014. https://doi.org/10.1007/s15007-014-0484-1

Diehl, K., Quick, C., Matthias-Maser, S., Mitra, S., Jaenicke, R.: The ice nucleating ability of pollen: Part I: Laboratory studies in deposition and condensation freezing modes. Atmospheric Research 58, 75–87, 2001. https://doi.org/10.1088/1748-9326/5/4/044015

Frenguelli, G.: Pollen structure and morphology, Advances in Dermatology and Allergology, 20, 200–204, 2003.

Freudenthaler,V., Esselborn, M.,Wiegner, M.,Heese, B., Tesche, M. and co-authors: Depolarization ratio profiling at severalwavelengths in pure Saharan dust during SAMUM 2006, *Tellus* 61B, 165–179, 2009.

Fröhlich-Nowoisky, J., Kampf, C. J., K., Weber, B., Huffman, J.A., Pöhlker, C., Andreae, M. O., Lang-Yona, N., et al.: Bioaerosols in the Earth system: Climate, health, and ecosystem interactions . Atmospheric Research, 182, 346-76, 2016. https://doi.org/10.1016/j.atmosres.2016.07.018.

Griffiths, P. T., Borlace, J.-S., Gallimore, P. J., Kalberer, M., Herzog, M., and Pope, F. D.: Hygroscopic growth and cloud activation of pollen: a laboratory and modelling study, Atmos. Sci. Lett., 13, 289–295, https://doi.org/10.1002/asl.397, 2012.

Haarig, M., Ansmann, A., Baars, H., Jimenez, C., Veselovskii, I., Engelmann, R., and Althausen, D.: Depolarization and lidar ratios at 355, 532, and 1064 nm and microphysical properties of

aged tropospheric and stratospheric Canadian wildfire smoke, Atm. Chem. Phys., 18, 11847–11861, 2018.

Heidemarie, S. U., Grímsson, F., Weber, M., Zetter, R., Hesse, M., Buchner, R., Svojtka, M., et Frosch-Radivo, A.:. *Illustrated Pollen Terminology*. 2e éd. Springer International Publishing, 2018. http://www.springer.com/gp/book/9783319713649.

Hu, Q., Goloub, P., Veselovskii, I., Bravo-Aranda, J.-A., Popovici, I., Podvin, T., Haeffelin, M., Lopatin, A. , Dubovik, O., Pietras, C., Huang, X., Torres, B., and Chen, C.: Long-range-transported Canadian smoke plumes in the lower stratosphere over northern France, Atmos. Chem. Phys. 19, 1173 – 1193, 2019. doi.org/10.5194/acp-19-1173-2019.

Immler, F., Engelbart, D., Schrems, O.: Fluorescence from atmospheric aerosol detected by a lidar indicates biogenic particles in the lower stratosphere, Atmos. Chem. Phys. 5, 345–355, 2005.

Katifori, E., Alben, S., Cerda, E., Nelson, D. R., and Dumais, J.: Foldable structures and the natural design of pollen grains, P. Natl. Acad. Sci. USA, 107, 7635–7639, https://doi.org/10.1073/pnas.0911223107, 2010.

Klett J.D., "Lidar inversion with variable backscatter/extinction ratios", Appl.Opt. 24, 1638-1643, 1985.

Lake, I.R., Jones, N.R., Agnew, M., Goodess, C.M., Giorgi, F., Hamaoui-Laguel, L., Semenov, M.A., Solomon, F., Storkey, J., Vautard, R., Epstein, M.M.: Climate Change and Future Pollen Allergy in Europe. Environ Health Perspect 125, 385–391, 2017. https://doi.org/10.1289/EHP173

Li, B., Chen, S., Zhang, Y., Chen, H., Guo, P.: Fluorescent aerosol observation in the lower atmosphere with an integrated fluorescence-Mie lidar, J. Quant. Spectr. Rad. Transf., 227, 211–218, 2019.

Mack, S. M., Madl, A. K., Pinkerton, K. E.: Respiratory health effects of exposure to ambient particulate matter and bioaerosols, *Comprehensive Physiology*, 10, 1-20, 2020. https://onlinelibrary.wiley.com/doi/abs/10.1002/cphy.c180040

Miyakawa, T., Kanaya, Y., Taketani, F., Tabaru, M., Sugimoto, N., Ozawa, Y., and Takegawa, N.: Ground-based measurement of fluorescent aerosol particles in Tokyo in the spring of 2013: potential impacts of nonbiological materials on autofluorescence measurements of airborne particles, J. Geophys. Res. Atmos., 120, 1171–1185, 2015, doi:10.1002/2014JD022189.

554 Müller, D., Mattis, I., Wandinger, U., Ansmann, A., Althausen, D., Stohl, A.: Raman lidar
555   observations of aged Siberian and Canadian forest fire smoke in the free troposphere over
556   Germany in 2003: Microphysical particle characterization, J. Geophys. Res., 110, D17201,
557   doi:10.1029/2004JD005756, 2005.

558 Nicolae D., A. Nemuc, D. Müller, C. Talianu, J. Vasilescu, L. Belegante, and A. Kolgotin:
559   Characterization of fresh and aged biomass burning events using multi-wavelength Raman
560   lidar and mass spectrometry, J. Geophys. Res. 118, 2956–2965, doi:10.1002/jgrd.50324, 2013.

561 Noh, M. Y., Müller, D., Lee, H., and Choi, T.: Influence of biogenic pollen on optical properties
562   of atmospheric aerosols observed by lidar over Gwangju, South Korea, Atmos. Environ., 69,
563   139–147, https://doi.org/10.1016/j.atmosenv.2012.12.018, 2013a

564 Noh, Y. M., Lee, H., Mueller, D., Lee, K., Shin, D., Shin, S., Choi, T. J., Choi, Y. J., and Kim, K.
565   R.: Investigation of the diurnal pattern of the vertical distribution of pollen in the lower
566   troposphere using LIDAR, Atmos. Chem. Phys., 13, 7619–7629, https://doi.org/10.5194/acp-
567   13-7619-2013, 2013b.

568 Pan, Y.-L.: Detection and characterization of biological and other organic-carbon aerosol particles
569   in atmosphere using fluorescence, J. Quant. Spectr. Radiat. Trans. 150, 12–35, 2015.

570 Pohlker, C.; Huffman, J.A.; Poschl, U. Autofluorescence of atmospheric bioaerosols-fluorescent
571   biomolecules and potential interferences. Atmos. Meas. Tech. **2012**, 5, 37–71.

572 Pope, F.D.: Pollen grains are efficient cloud condensation nuclei. Environ. Res. Lett. 5, 044015,
573   2010. https://doi.org/10.1088/1748-9326/5/4/044015

574 Rao, Z., He, T., Hua D, Wang, Y., Wang, X., Chen, Y., Le J.: Preliminary measurements of
575   fluorescent aerosol number concentrations using a laser-induced fluorescence lidar, Appl. Opt.
576   57, 7211-7215, 2018.

577 Reichardt, J.: Cloud and aerosol spectroscopy with Raman lidar, J. Atm. Ocean. Tech., 31, 1946-
578   1963, 2014.

579 Reichardt, J., Leinweber, R., Schwebe, A.: Fluorescing aerosols and clouds: investigations of co-
580   existence, Proceedings of the 28th ILRC, Bucharest, Romania, 25-30 June, 2017.

581 Richardson, S.C., Mytilinaios, M., Foskinis, R., Kyrou, C., Papayannis, A., Pyrri, I., Giannoutsou,
582   E., Adamakis, I.D.S.: Bioaerosol detection over Athens, Greece using the laser induced
583   fluorescence technique, Science of the Total Environment 696, 133906, 2019.
584   https://doi.org/10.1016/j.scitotenv.2019.133906

585 Saito, Y., Ichihara, K., Morishita, K., Uchiyama, K., Kobayashi, F., Tomida, T.: Remote detection
586   of the fluorescence spectrum of natural pollens floating in the atmosphere using a laser-
587   induced-fluorescence spectrum (LIFS) lidar, Remote Sens., 10, 1533, 2018.
588   doi:10.3390/rs10101533.

589 Sassen, K.: Boreal tree pollen sensed by polarization lidar: Depolarizing biogenic chaff, Geophys.
590   Res. Lett., 35, L18810, https://doi.org/10.1029/2008GL035085, 2008.

591 Sassen, K.: Elliptical pollen corona from North American boreal paper birch trees (Betula
592   papyrifera): strong fall orientations for near-spherical particles, Appl. Opt., 50, F1–F5,
593   https://doi.org/10.1364/AO.50.0000F1, 2011.

594 Shang, X., Giannakaki, E., Bohlmann, S., Filioglou, M., Saarto, A., Ruuskanen, A., Leskinen, A.,
595   Romakkaniemi, S., Komppula, M.: Airborne pollen observations using a multi-wavelength
596   Raman polarization lidar in Finland: characterization of pure pollen types, Atm. Chem. Phys.,
597   20, 15323–15339, 2020. doi.org/10.5194/acp-20-15323-2020.

598 Sofiev, M., Vira, J., Kouznetsov, R., Prank, M., Soares, J., Genikhovich, E.: Construction of the
599   SILAM Eulerian atmospheric dispersion model based on the advection algorithm of Michael
600   Galperin. Geoscientific Model Development 8, 3497–3522, 2015.
601   https://doi.org/10.5194/gmd-8-3497-2015

602 Sicard, M., Izquierdo, R., Alarcón, M., Belmonte, J., Comerón, A., and Baldasano, J. M.: Near-
603   surface and columnar measurements with a micro pulse lidar of atmospheric pollen in
604   Barcelona, Spain, Atmos. Chem. Phys., 16, 6805–6821, https://doi.org/10.5194/acp-16-6805-
605   2016, 2016.

606 Stein, A.F., Draxler, R.R, Rolph, G.D., Stunder, B.J.B., Cohen, M.D., and Ngan, F.: NOAA's
607   HYSPLIT atmospheric transport and dispersion modeling system, Bull. Amer. Meteor. Soc.,
608   96, 2059-2077, 2015. http://dx.doi.org/10.1175/BAMS-D-14-00110.1

609 Steiner, A. L., Brooks, S. D., Deng, C., Thornton, D. C.O., Pendleton, M. W., Bryant, V:. Pollen
610   as atmospheric cloud condensation nuclei, *Geophysical Research Letters*, 2015GL064060,
611   2015. https://doi.org/10.1002/2015GL064060.

612 Sugimoto, N. and Lee, C. H.: Characteristics of dust aerosols inferred from lidar depolarization
613   measurements at two wavelength, Appl. Opt., 45, 7468–7474, 2006.

614 Sugimoto, N., Huang, Z., Nishizawa, T., Matsui, I, Tatarov, B.: Fluorescence from atmospheric
615   aerosols observed with a multichannel lidar spectrometer," Opt. Expr. 20, 20800-20807, 2012.

616 Tesche, M., Ansmann, A., Müller, D., Althausen, D., Engelmann, R., Freudenthaler, V., and Groß,

617   S.: Vertically resolved separation of dust and smoke over Cape Verde using multiwavelength

618   Raman and polarization lidars during Saharan Mineral Dust Experiment 2008, J. Geophys.

619   Res., 114, D13202, doi:10.1029/2009JD011862, 2009.

620 Veselovskii, I., Whiteman, D. N., Korenskiy, M., Suvorina, A., Kolgotin, A., Lyapustin, A., Wang,

621   Y., Chin, M., Bian, H. Kucsera, T. L., Perez-Ramirez, D., Holben, B.: Characterization of

622   forest fire smoke event near Washington, D.C. in Summer 2013 with multi-wavelength lidar.

623   Atmos. Chem. Phys. 15, 1647–1660, 2015.

624 Veselovskii, I., Hu, Q., Goloub, P., Podvin, T., Korenskiy, M., Pujol, O., Dubovik, O., Lopatin,

625   A.: Combined use of Mie-Raman and fluorescence lidar observations for improving aerosol

626   characterization: feasibility experiment, Atm. Meas. Tech., 13, 6691–6701, 2020.

627   doi.org/10.5194/amt-13-6691-2020a.

628 Veselovskii, I., Hu, Q., Goloub, P., Podvin, T., Korenskiy, M., Derimian, E., Legrand, M.,

629   Castellanos, P.: Variability of Lidar-Derived Particle Properties Over West Africa Due to

630   Changes in Absorption: Towards an Understanding. Atm. Chem. Phys., 20, 6563-6581, 2020b.

631   doi.org/10.5194/acp-20-6563-2020

632

633

634 **Figures**

635
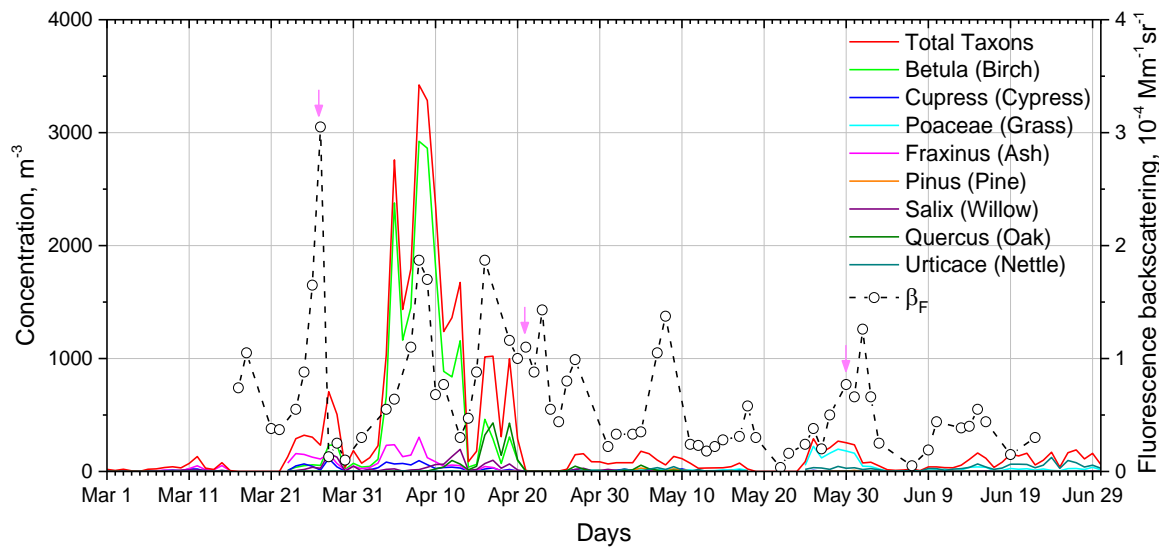
636   Fig.1. Daily concentration of most abundant pollen taxa, for the period March–June 2020 in Lille

637   from in situ measurements on the rooftop. Open symbols show fluorescence backscattering β_F

638   measured by lidar. Lidar measurements are averaged over night and maximal value in 500–1000

639   m range is shown. Vertical arrows mark the sessions, which are further analyzed in Fig.8, 10, 11.

640

641

642

643

644
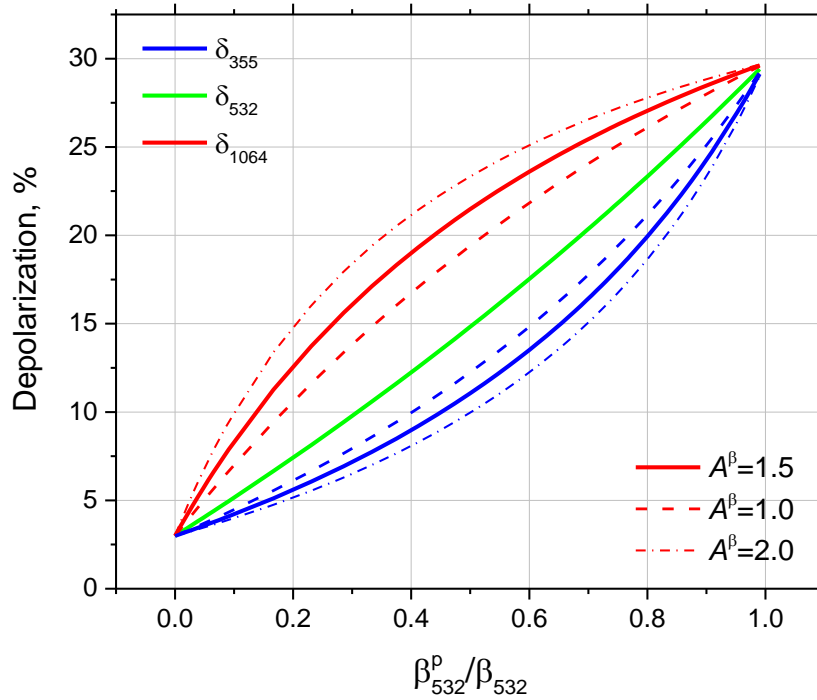
645 Fig.2. Depolarization ratios at 355, 532 and 1064 nm as a function of pollen contribution to the

646 total backscattering coefficient $\frac{\beta^{p}_{532}}{\beta_{532}}$. Depolarization ratios of pollen (δ^{p}) and background aerosol

647 (δ^{b}) are assumed to be spectrally independent δ^{p}=30% and δ^{b}=3%. Backscattering coefficient of

648 pollen is spectrally independent. The backscattering Angstrom exponents of background aerosol

649 were assumed to be the same for both pairs of wavelengths ($A^{\beta}_{355/532} = A^{\beta}_{532/1064}$), and results are

650 shown for the values A^{β}=1.0, 1.5, 2.0.

651

652

653

654
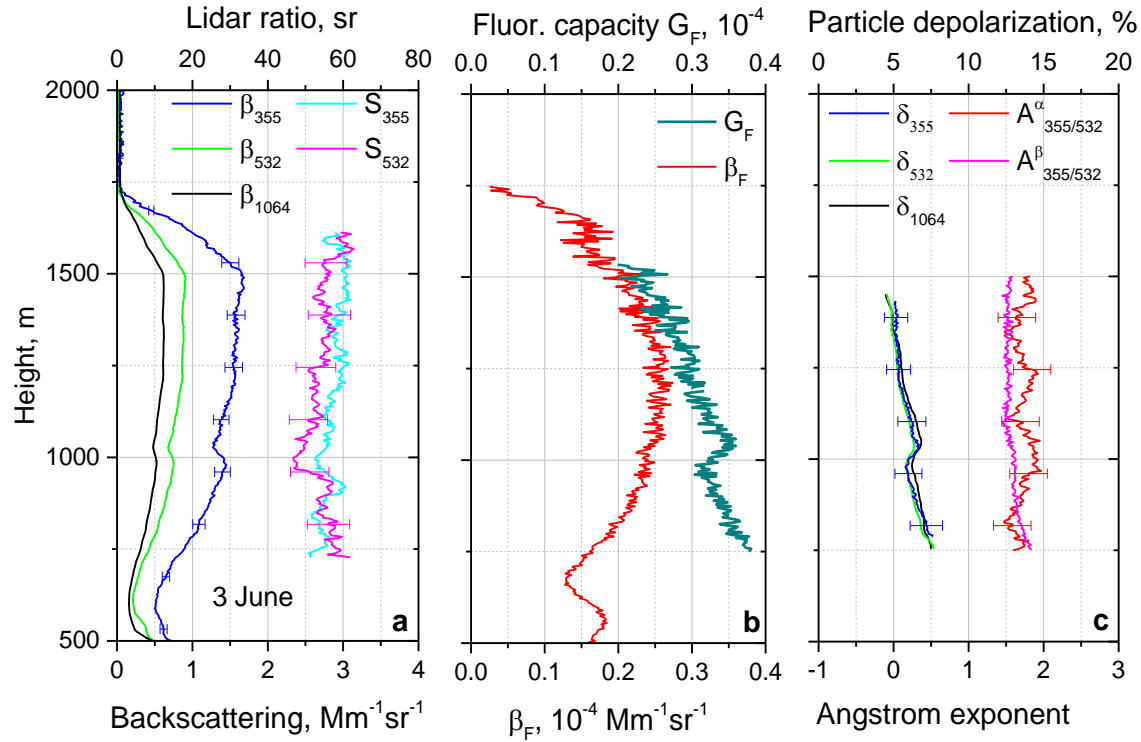
Fig.3. Measurements in the condition of background aerosol predominance. Vertical profiles of (a) backscattering coefficients β_{355}, β_{532}, β_{1064} and lidar ratios S_{355}, S_{532}; (b) fluorescence backscattering β_F and fluorescence capacity $G_F = \beta_F/\beta_{532}$; (c) particle linear depolarization ratios δ_{355}, δ_{532}, δ_{1064} together with extinction and backscattering Angstrom exponents $A^{\alpha}_{355/532}$, $A^{\beta}_{355/532}$ on 3 June 2020 for 20:30 – 23:00 UTC. Measurements were performed at 30 degree to the horizon.

660

661

662

663

664

665

666

667
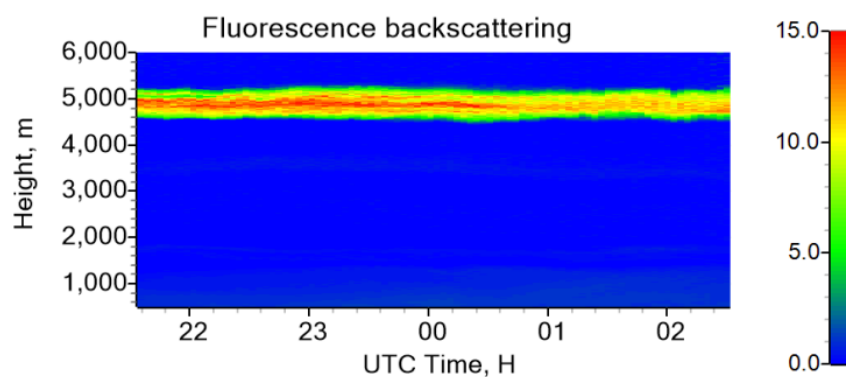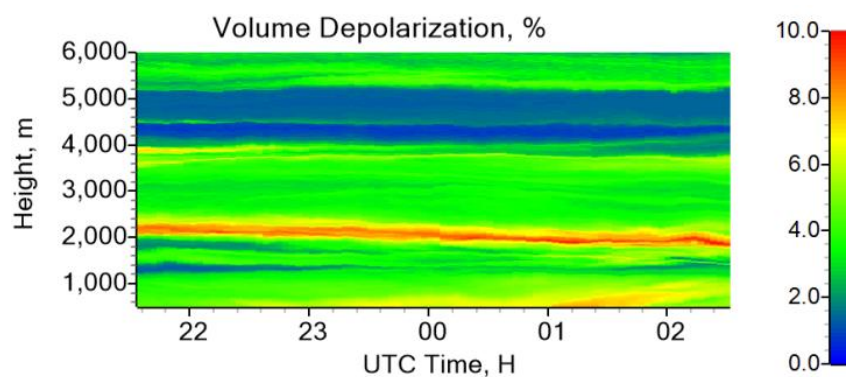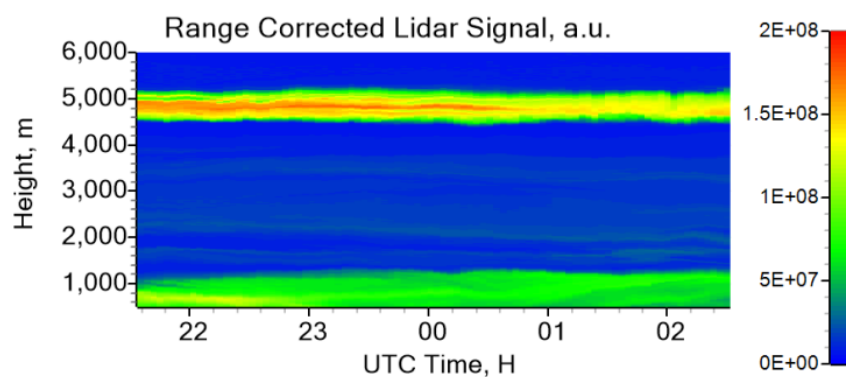
Fig.4. Range corrected lidar signal at 1064 nm, volume depolarization ratio at 1064 nm and fluorescence backscattering coefficient (in 10^{-4} $Mm^{-1}sr^{-1}$) on 23-24 June 2020.

670

671

672
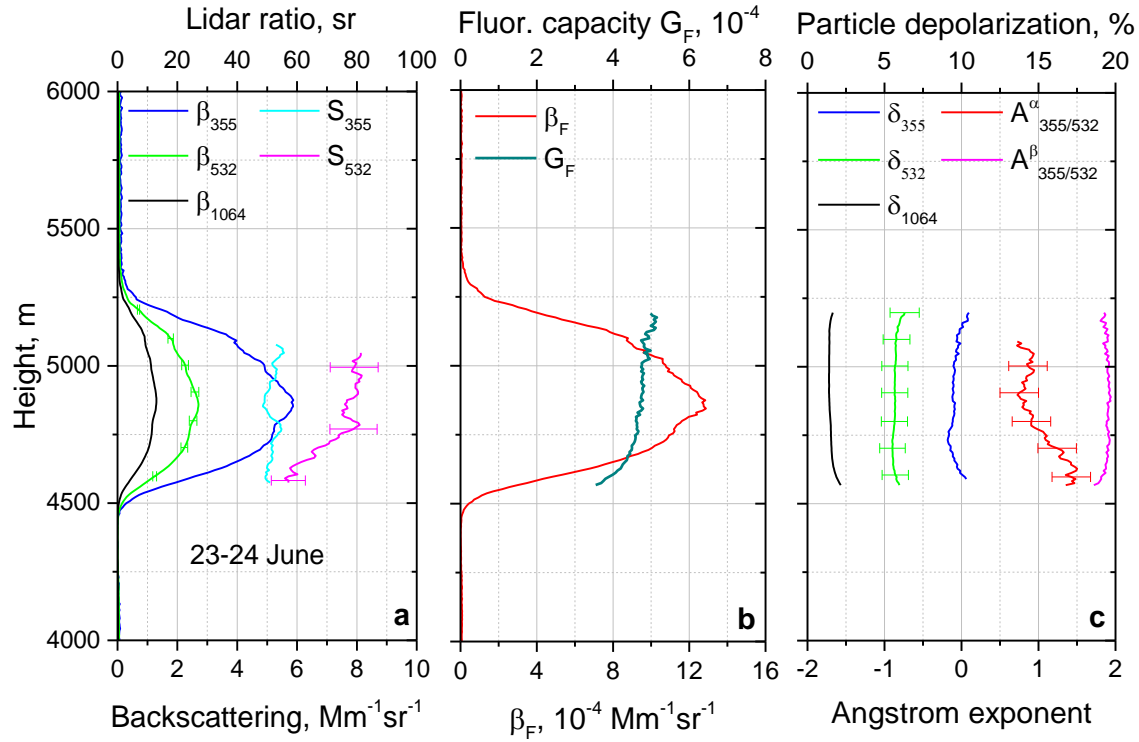
673

674 Fig.5. Vertical profiles of (a) backscattering coefficients β_{355}, β_{532}, β_{1064}, lidar ratios S_{355}, S_{532}; (b)

675 fluorescence backscattering coefficient β_F, fluorescence capacity G_F; and (c) particle

676 depolarization ratios δ_{355}, δ_{532}, δ_{1064} together with the extinction and backscattering Angstrom

677 exponents $A^{\alpha}_{355/532}$, $A^{\beta}_{355/532}$ on the night 23-24 June 2020 for 21:30 – 02:30 UTC.

678

679

680
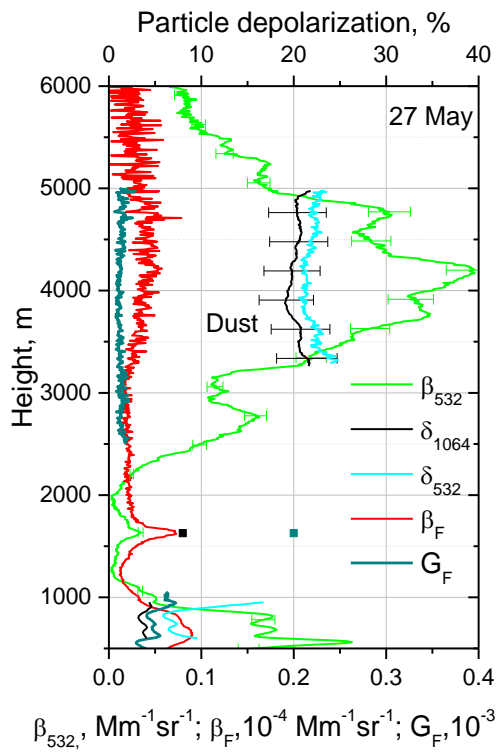
681

682   Fig.6. Lidar measurements during dust episode. Vertical profiles of particle β_{1064} and fluorescence

683   β_F backscattering coefficients, fluorescence capacity G_F and particle depolarization ratios δ_{1064},

684   δ_{532} on 27 May 2020 for 21:00–23:00 UTC.

685

686

687

688

689
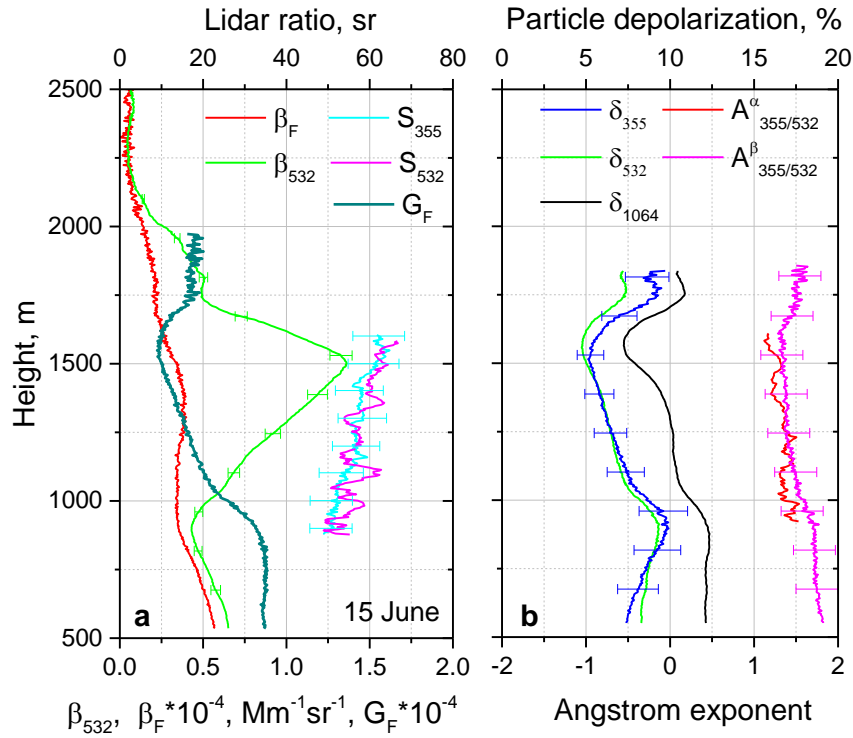
Fig.7. Lidar measurements in the condition of the aerosol hygroscopic growth in 900-1500 m height range. Vertical profiles of (a) particle β_{532} and fluorescence β_F backscattering coefficients, fluorescence capacity G_F, lidar ratios S_{355}, S_{532} and (b) particle depolarization ratios δ_{355}, δ_{532}, δ_{1064} together with extinction $A^{\alpha}_{355/532}$ and backscattering $A^{\beta}_{355/532}$ Angstrom exponents measured on 15 June 2020 for 22:00 – 24:00 UTC.

695

696

697

698
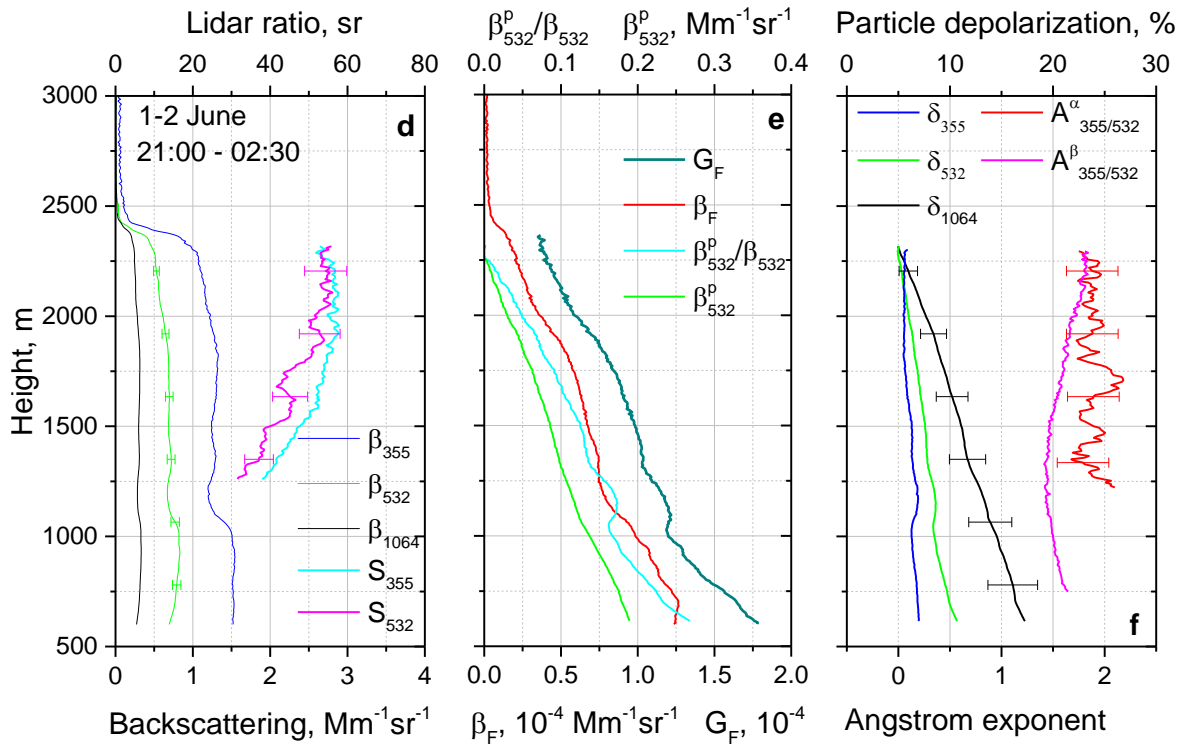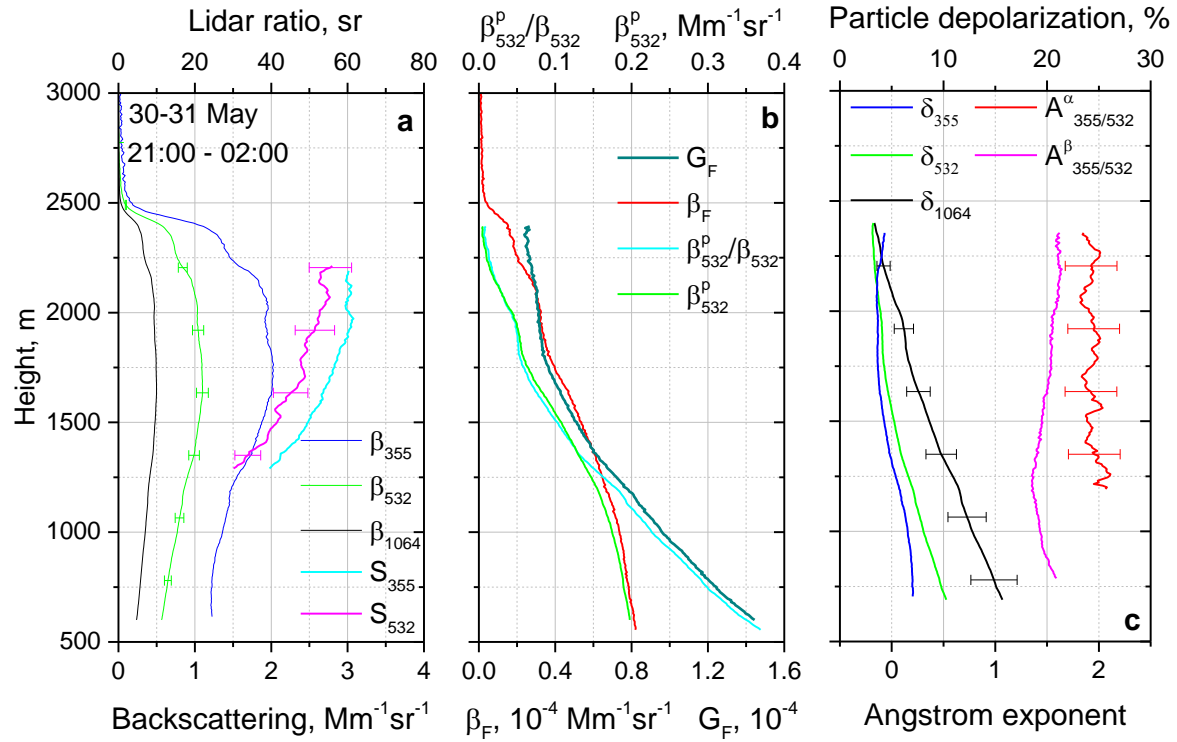
699   Fig.8. Vertical profiles of (a, d) particle backscattering coefficients β_{355}, β_{532}, β_{1064} and lidar ratios

700   S_{355}, S_{532}, (b, e) fluorescence backscattering coefficient β_F, fluorescence capacity G_F, pollen

701 backscattering coefficient β^p_{532} and its contribution to the total backscattering $\dfrac{\beta^p_{532}}{\beta_{532}}$; (c, f) particle

702 depolarization ratios δ_{355}, δ_{532}, δ_{1064} together with extinction $A^{\alpha}_{355/532}$ and backscattering $A^{\beta}_{355/532}$

703 Angstrom exponents on (a-c) 30 - 31 May 2020 for 21:00 – 02:00 UTC and on (d-f) 1-2 June 2020

704 for 21:00 – 02:30 UTC. Profiles of β^p_{532} and $\dfrac{\beta^p_{532}}{\beta_{532}}$ were computed in assumption of $\delta^p_{532} = 30\%$.

705 The depolarization ratios of the background aerosol δ^b_{532} are measured/assumed to be 3% on 30

706 May and 5% on 1 May.

707

708

709

710

711

712

713

714

715

716

717

718

719

720

721

722

723

724
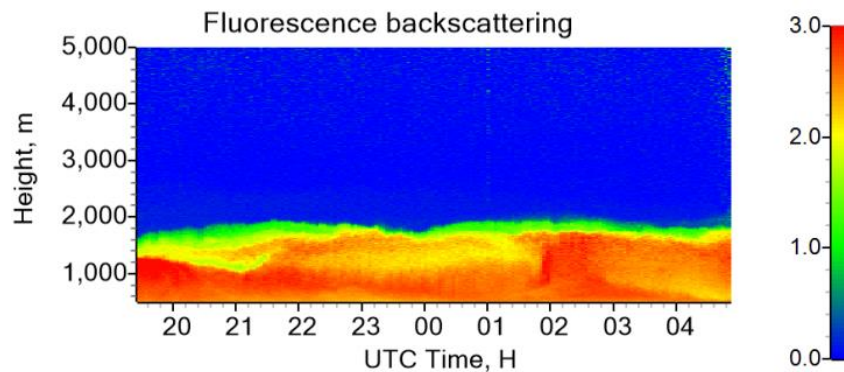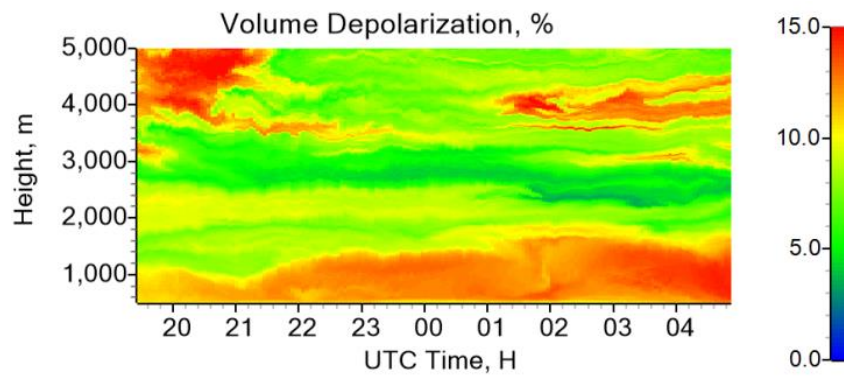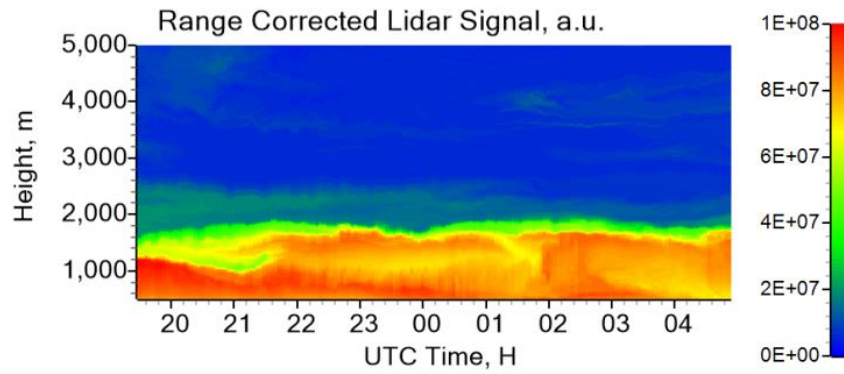
Fig.9. Range corrected lidar signal at 1064 nm (upper panel), volume depolarization ratio at 1064

nm (middle panel) and fluorescence backscattering coefficient (in 10^{-4} $Mm^{-1}sr^{-1}$, lower panel)

measured on 27-28 March 2020.

729

730
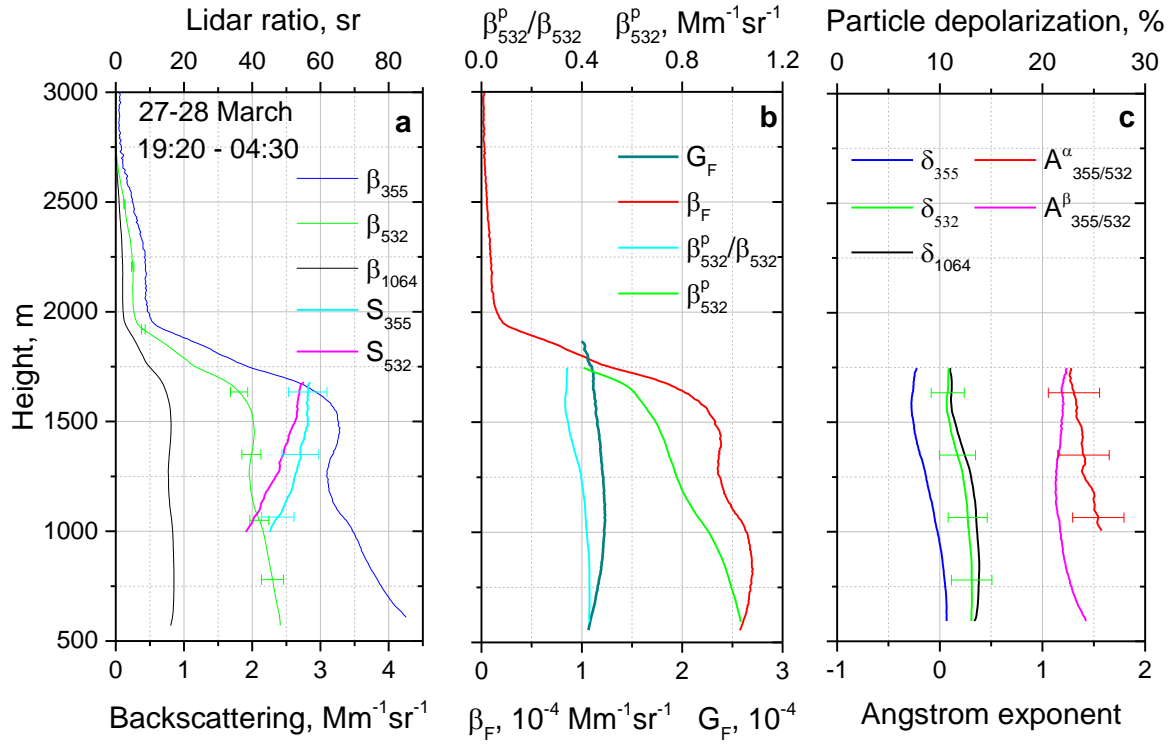
Fig.10. Vertical profiles of (a) particle backscattering coefficients β_{355}, β_{532}, β_{1064} and lidar ratios S_{355}, S_{532}; (b) fluorescence backscattering coefficient β_F, fluorescence capacity G_F, pollen backscattering coefficient β_{532}^p and its contribution to the total backscattering $\dfrac{\beta_{532}^p}{\beta_{532}}$; (c) particle depolarization ratios δ_{355}, δ_{532}, δ_{1064} together with extinction $A_{355/532}^{\alpha}$ and backscattering $A_{355/532}^{\beta}$ Angstrom exponents measured on 27 - 28 March 2020 for19:20 – 04:30 UTC. Profiles of β_{532}^p and $\dfrac{\beta_{532}^p}{\beta_{532}}$ were computed in assumption of $\delta_{532}^p = 30\%$ and $\delta_{532}^b = 3\%$.

737

738
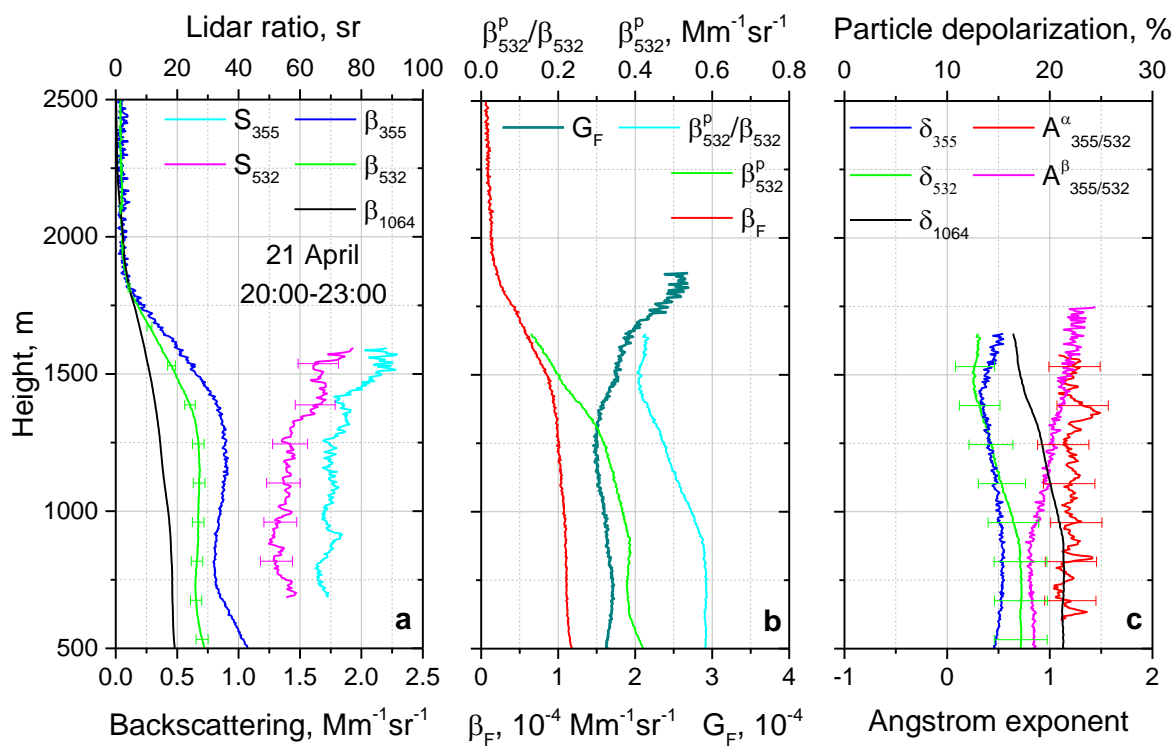
739

740 Fig.11. The same particle parameters as in Fig.10 for 21 April 2020, 20:00-23:00 UTC.
741 Measurements were performed at 30 deg to horizon.

742
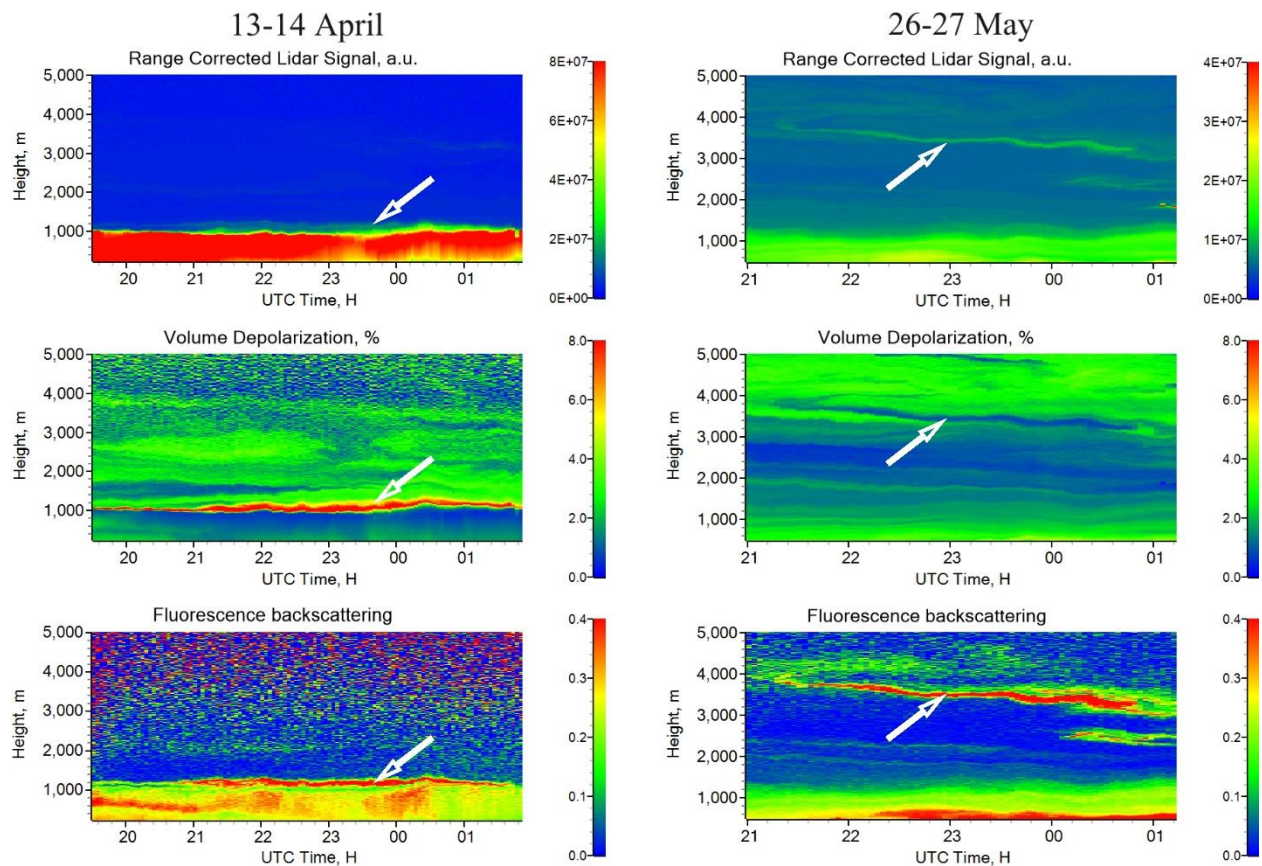
743 Fig.12. Range corrected lidar signal at 1064 nm, volume depolarization ratio δ^v_{1064} and

744 fluorescence backscattering coefficient (in 10^{-4} $Mm^{-1}sr^{-1}$) measured on 13-14 April (left column)

745 and 26-27 May 2020 (right column). Arrows point to the fluorescent layers.

746

747

748
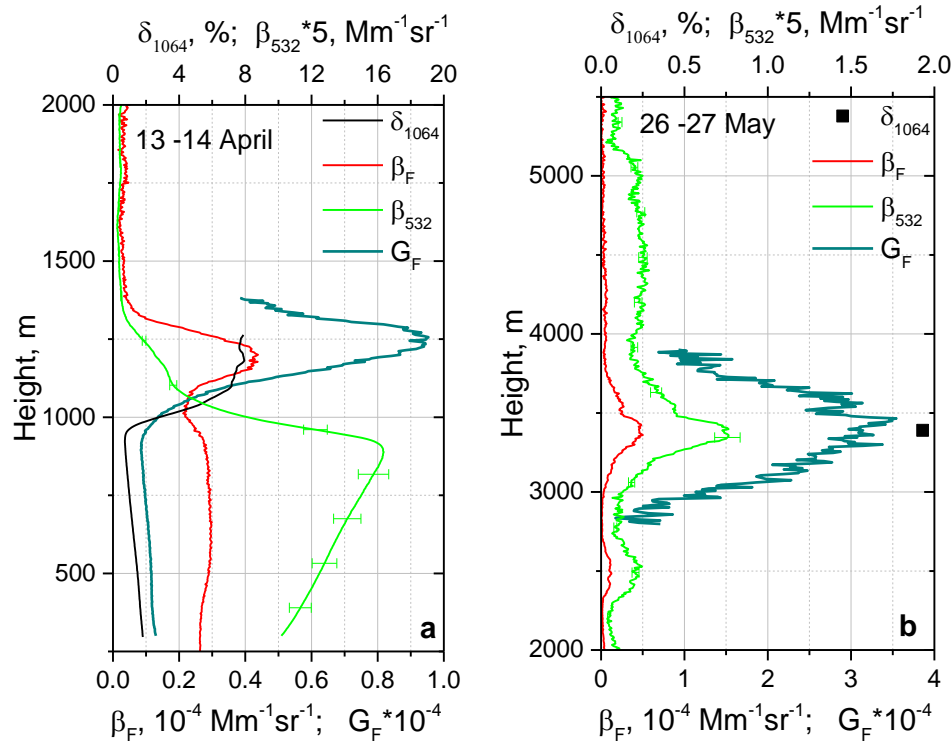
749

750 Fig.13. Vertical profiles of elastic β_{532} and fluorescence β_F backscattering coefficients,
751 fluorescence capacity G_F and particle depolarization ratio δ_{1064} measured on (a) 13-14 April for
752 21:00 – 01:00 UTC and (b) 26-27 May 2020 for 23:30 – 00:40 UTC. Values of β_{532} are multiplied
753 by factor 5.

754

755

756

757
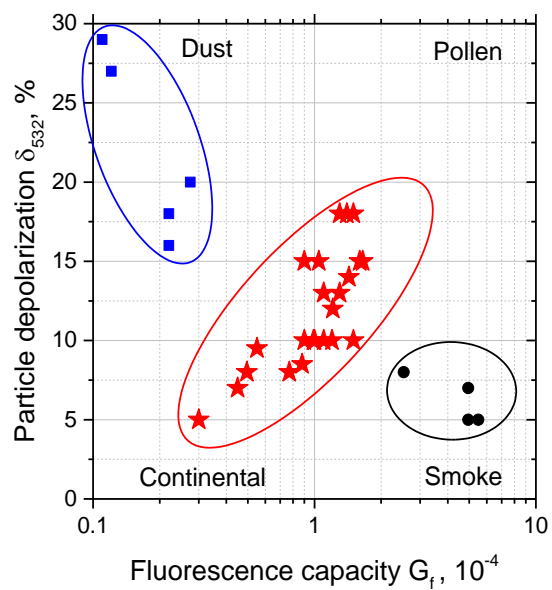
758

759 Fig.14. Particle depolarization δ_{532} versus fluorescence capacity G_F. This diagram allows to
760 identify dust (blue), smoke particles (black) and aerosol mixtures containing pollen (red).

761

762